Modelling and optimization of UV absorbing photovoltaic windows using a thin film AlN:Eu^{3+} luminescence library

Merkx, Evert P.J.; Lensvelt, Thomas G.; van der Kolk, Erik

DOI
10.1016/j.solmat.2019.110032

Publication date
2019

Document Version
Final published version

Published in
Solar Energy Materials and Solar Cells

Solar Energy Materials and Solar Cells 200 (2019) 110032

Contents lists available at ScienceDirect

Solar Energy Materials and Solar Cells

journal homepage: www.elsevier.com/locate/solmat

Modelling and optimization of UV absorbing photovoltaic windows using a thin film AlN:Eu^{3+} luminescence library

Evert P.J. Merkx*, Thomas G. Lensvelt, Erik van der Kolk

Luminescence Materials, Delft University of Technology, Mekelweg 15, Delft, 2629 JB, the Netherlands

ARTICLE INFO

Keywords:
Combinatorial science
AlN
Europium
Sputter deposition
Solar-conversion
Luminescent solar concentrator

ABSTRACT

Building-integrated photovoltaics are drawing much attention to make the built environment self-sufficient in terms of electricity. Luminescent solar concentrators (LSCs) can provide this electricity generation when used as photovoltaic windows. Paramount to an efficient LSC are non-overlapping absorption and emission spectra, to avoid self-absorption. This non-overlap can be achieved by absorbing incoming UV light and emitting in the red to infrared. In this article, we present a technique for optimizing LSCs without self-absorption, using Eu^{3+}-doped AlN as a model system. The parameters affecting light absorption, emission and transport are extracted from a combinatorially sputtered gradient material library. This library results from a single deposition, with a gradient in thickness and Eu concentration. AlN:Eu^{3+} absorbs strongly until 450 nm, with a peak solar absorption of 499 cm^{-1} $at\%^{-1}$ at 350 nm due to a charge transfer band. The strongest emission is at 622 nm, thereby exhibiting no self-absorption. The presented optimization model strikes a balance between concentration quenching and absorptivity of Eu dopants by using the parameters extracted from the material library. For thicker films, concentration quenching can be avoided by using a lower dopant concentration, while still outperforming thinner films due to fast increasing absorption. The results demonstrate that, while AlN:Eu^{3+} itself should only be viewed as a model system, thin films doped with rare earths can yield industry-compatible, high efficiency LSCs because of their high absorption coefficients and lack of self-absorption.

1. Introduction

Building-integrated photovoltaics (BIPVs) can turn the passive building envelope into a source of electricity. For example, when utilizing the principle of a luminescent solar concentrator (LSC), luminescent thin films on window glass can transform these windows into electricity generating surfaces. Fig. 1a shows the working principle of a thin film LSC. Sunlight incident on the window is captured by luminescent centers in the coating on the window, which convert the captured light to a different wavelength. The converted light is emitted isotropically. Light emitted at an angle larger than the critical angle of the LSC is then waveguided through the LSC towards the windowpane by total internal reflection. In the windowpane PV cells are placed, which face the edges of the LSC. These cells convert the waveguided light into electricity. The light absorbed by the LSC is effectively concentrated on the PV cells. The area covered by the PV cells is therefore very small compared to the large LSC surface. In addition, the cells only need to be optimized for the LSC emission, a much narrower range of wavelengths than the solar spectrum. Therefore, the PV cells can have unity external quantum efficiency (EQE) at the LSC emission wavelengths. LSCs could replace ordinary windows as transparent energy generating BIPV at no high additional investment and no wiring blocking the view.

The concept of LSCs has existed since the 1970s [1], but wide adaptation was mainly impeded by these LSCs displaying bright coloration, making them unsuitable for use as windows in the building envelope. A recent development in LSCs is to use materials that absorb in the ultraviolet (UV) and have a large Stokes' shift [2–4]. This combination leads to high transmission in the visible spectrum, and emission in the red to near infrared (NIR), yielding the appearance of an ordinary window without coloring. Another advantage of this non-overlapping absorption and emission is that no parasitic absorption of the luminescence center itself (self-absorption) occurs. The absence of self-absorption means that when a photon is emitted under total internal reflection (in a perfect waveguide), it will reach the perimeter of the LSC, regardless of the LSC's size. The absence of self-absorption is therefore of great importance to the overall efficiency of the LSC.

Optimization of the composition of the luminescent coating is often a laborious process. The light-conversion efficiency of the LSC material has to be measured for many individual samples with differing

* Corresponding author.
E-mail address: e.p.j.merkx@tudelft.nl (E.P.J. Merkx).

https://doi.org/10.1016/j.solmat.2019.110032
Received 30 December 2018; Received in revised form 19 June 2019; Accepted 28 June 2019

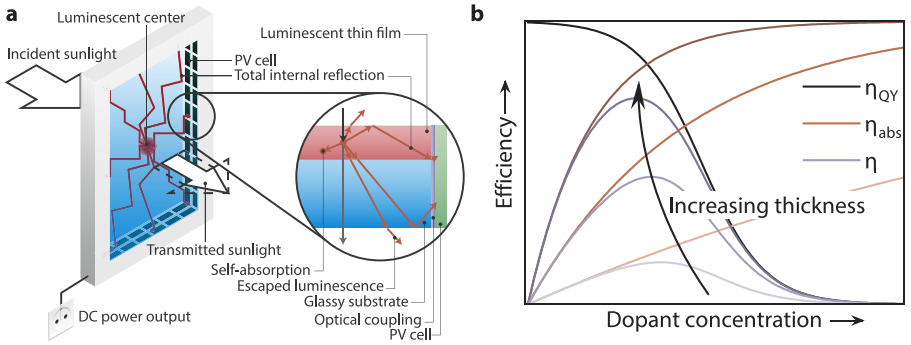

Fig. 1. a) Schematic of the workings of a thin film luminescent solar concentrator. b) Sketch of the influence of changing thickness or dopant concentration on the individual and overall LSC efficiencies.

compositions. To overcome this laborious optimization, another approach is to fabricate thin film libraries of LSC materials using combinatorial gradient magnetron sputtering [5]. With combinatorial gradient magnetron sputtering, a single substrate from a single deposition provides many compositions (a composition library) that can all be characterized automatically. Additionally, magnetron sputtering is already commonly used for window coatings [6]. The optimal composition found by this gradient method can therefore be implemented in glass coating on an industrial scale with relative ease.

In this work, we want to optimize the optical efficiency of an LSC without self-absorption based on experimental data from a composition library. As a model system for materials absorbing in the UV and having emission in the red to NIR, a good choice for a thin film LSC coating is Eu^{3+}-doped AlN. AlN:Eu^{3+} can be excited by light below 400 nm, shows strong emission at 600 nm–625 nm at room temperature [7–9], can be coated on glass through sputter deposition [10], and is chemically inert [11].

The optical efficiency of an LSC can be described with [12]

$$\eta_{opt} = (1 - R)\eta_{abs}\eta_{QY}\eta_{trap}\eta_{WG}\eta_{SA}. \quad (1)$$

Here, each factor describes one step in the light conversion-concentration process. $1 - R$ describes the amount of light transmitted into the film. η_{abs} is the fraction of transmitted light absorbed by the luminescent particles. η_{QY} is the internal photoluminescent quantum efficiency of Eu^{3+}, i.e. the ratio of photons emitted to photons absorbed by Eu^{3+}. η_{trap} is the fraction of emitted photons that remain trapped within the LSC through total internal reflection. η_{WG} describes the efficiency of the waveguiding of light to the perimeter of the LSC. η_{WG} can be affected by scattering losses and absorption by the waveguide. η_{SA} is a factor to take self-absorption into account.

Assuming an optical density of 0.8 and an index of refraction of $n = 2$, a UV-absorbing LSC without self-absorption could have an optical efficiency of 2.3 to 5.8% when $\eta_{QY} = 1$. This value is highly dependent on where the absorption maximum of the LSC lies. When this maximum lies to the visible spectrum, the amount of photons in the solar spectrum increases tremendously. In practice, these optical efficiencies are not attained with UV-absorbing LSCs due to low η_{QY} of typically $\sim$ 10% for quantum dots, to $\sim$ 80% for dye molecules.

The product $\eta_{abs} \times \eta_{QY}$, shown in Fig. 1b, is crucial to the overall performance of an LSC. When the concentration of luminescent centers is low, η_{QY} tends to be high, but at the same time, η_{abs} is low due to the low amount of absorbing centers. Conversely, at higher concentrations, η_{abs} is high due to many absorbing centers, but η_{QY} drops as a consequence of concentration quenching [13]. Apart from the dopant concentration within the film, the film thickness (at equal dopant concentration) will increase η_{abs} (to a first order, when disregarding interference effects). The optimum for $\eta_{abs} \times \eta_{QY}$ is therefore also specific to the thickness of the luminescent layer. As industrial throughput decreases (and cost increases) with increasing film thickness, it is of great importance to establish methods that can find the optimal dopant concentration for the desired thickness.

In this work, we present a general approach that only requires the deposition of a single thin film to optimize $\eta_{abs} \times \eta_{QY}$. We do this optimization in three steps. Firstly, we deposit a film with a thickness- and a Eu concentration gradient, employing off-axis combinatorial sputtering of Al and Eu sources in a reactive $O_2 + N_2 + Ar$ atmosphere. Here O_2 is added as dopant, which reduces the need for heat treatments to improve the intensity of the luminescence. Secondly, we determine the composition-dependent thickness, index of refraction, absorption, and quantum efficiency through a combination of energy-dispersive X-ray spectroscopy (EDX) and automated mapping of the transmission and laser-excited luminescence properties of the thin film. Thirdly, using the parameters extracted from the gradient thin film, we maximize the optical efficiency of AlN:Eu^{3+} thin film LSCs as a function of both thickness and Eu concentration, through optics simulations employing the transfer-matrix method.

2. Experimental

Library creation. The AlN:Eu thin film library was deposited on a square 44 × 44 mm^2 UV fused silica substrate (PGO) within an AJA ATC Orion 5 magnetron sputtering system (Fig. 2) with a base pressure of 1×10^{-9} bar. Prior to the deposition, the substrate had been cleaned by rinsing three times with DI water and ethanol, followed by a 15 min bath in an ultrasonic cleaner with DI water. The deposition was carried out with 5.08 cm diameter metal Al (99.9995%, Lesker) and Eu (99.99%, Demaco) targets, which were reactively co-sputtered with

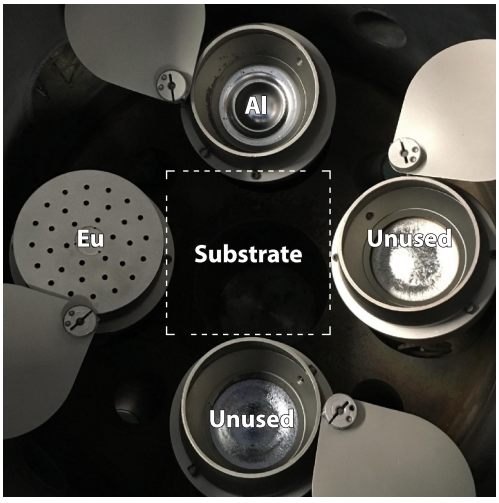

Fig. 2. Top-down photograph of the inside of the sputtering chamber, with the sources used for fabrication; the right and bottom sources are not used for fabrication.

respectively 150 W and 32 W RF power for 12.5 h. The deposition rate of Eu was reduced by a stainless steel mask with a pattern of concentric holes, blocking 88% of the surface of the Eu target. The process gas flow consisted of 18 sccm 6 N purity Ar, 0.25 sccm 5 N purity O_2 and 13.75 sccm 5 N purity N_2 into the sputtering chamber at a working pressure of 4×10^{-3}mbar. Oxygen was included in small amounts to the sputtering gas, and therefore to AlN, as alternative to thermal treatments at high temperatures [14]. O_2 and N_2 were introduced next to the substrate, while Ar was introduced at the Al source. Just before deposition, the substrate was heated to 400°C. During the deposition, the sample was not actively heated. The cooling of the sample during deposition can be seen in Fig. S1 in the Supplementary Materials. To realize a thin film with both a gradient in Eu and in film thickness, the substrate was sputtered without rotation.

Following the deposition, the luminescence of the library was improved by subsequently heating to 300°C and 500°C, both for 20 min, in a Solaris 150 rapid thermal processing (RTP) system. The RTP system was flushed with 9 standard liters per minute (SLM) N_2 (5 N purity) during the entire annealing procedure. Fig. S2 shows that this annealing treatment yields a 12-fold improvement in luminescence.

An undoped AlN reference sample was made with identical treatment, but with the Eu source switched off.

Composition analysis. A JEOL IT-100, operated at 15 keV with probing current at 70%, was used for SEM/EDX analysis. Quantitative elemental analysis without a conductive coating was achieved by employing the device in low vacuum mode (35 Pa pressure). Elemental compositions were quantified at 3000× magnification (31×23 μm^2 measurement area). XRD measurements were performed using a PANalytical X'pert Pro MPD diffractometer in Bragg-Brentano geometry, with a Cu Kα anode ($\lambda = 0.1540598$ nm) operating at 45 kV and 40 mA. The area illuminated by the X-ray beam was around 1×5 mm^2 in size.

Optical characterization. The total transmission was measured by placing the samples between a collimated (2.7 mm diameter) xenon light source and the entrance port of a 5.08 cm diameter integrating sphere (IS200-4, Thorlabs), with an Ocean Optics QEPro spectrometer (200 μm slit width) connected to the off-axis detector port. The samples were moved through the collimated beam with a sample holder placed on top of two stacked Thorlabs DDSM100 linear translation stages. Transmission spectra were recorded across the samples at 16×16 positions with a step size of 2.6 mm. Each position is recorded with an integration time of 250 ms and averaged 32×. Dark spectra were recorded by blocking the entrance of the integrating sphere with highly absorbing and reflecting Al tape. Lamp spectra were recorded by directly exposing the integrating sphere to the collimated light. The presented transmission spectra were corrected using these two reference measurements, measured with identical settings.

Photoluminescent excitation, emission, and decay measurements were carried out with a home-built *xy*-scanner setup, as described in Ref. [5]. An Ekspla NT230 OPO Laser was used as excitation source, operated at excitation wavelengths ranging from 210 nm to 420 nm in steps of 0.25 nm. Combined emission/excitation spectra were integrated for 300 ms and averaged 4× per excitation wavelength. These spectra were recorded with an Ocean Optics QE65000 spectrometer with a 100 μm entrance slit. A 430 nm longpass filter (Semrock) was used to remove reflected laser light. The emission was corrected for the quantum efficiency and non-linearity of the detector. For decay studies, the emission, filtered with a 355 nm longpass filter, was passed directly to a Hamamatsu R7600U-03 PMT operating at −600 V linked to a CAEN DT5730 Digitizer with 64 ns per channel. The sample was excited at 350 nm, with the laser pulsing at 50 Hz. Decay traces were collected over 200 laser pulses at 20×20 locations across the film, with 2 mm between steps.

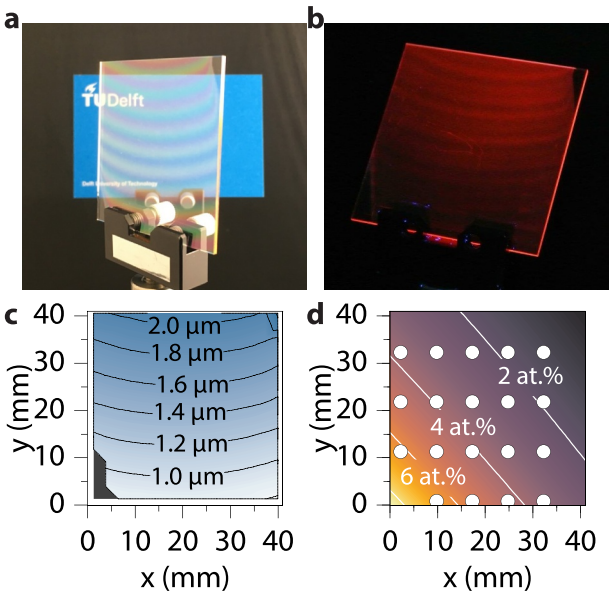

Fig. 3. Concentration library of AlN doped with Eu. Photographs of the library under a) white light with a colored background, b) UV illumination (250 nm) on a dark background, after annealing. The white dashed line indicates the presence of a luminescence optimum. c) Thickness across the film. d) Distribution of the Eu concentration across the substrate (RMSE<0.2 at.%), based on 24 local EDX measurements, marked by the white dots. (For interpretation of the references to colour in this figure legend, the reader is referred to the web version of this article.)

3. Results and discussion

Fig. 3a and Fig. 3b show the final product: a thin film, transparent in the visible spectrum, but with red emission when excited by UV light. The interference fringes are a consequence of the thickness gradient of the film, which ranges from 0.8 μm to 2.1 μm, as reported in Fig. 3c. The thickness is retrieved from fitting 16×16 local transmission measurements (see Fig. S4) to an extended Sellmeier model, as presented in Ref. [15]. A low Eu concentration is already indicated by the thickness measurement. If the Eu concentration was high, the shape of the thickness gradient would more follow the cosine distribution caused by the Eu source. In this case, the thickness directly follows the cosine sputtering distribution dictated by the Al source.

EDX measurements provide the local chemical composition of the gradient thin film at 24 positions, shown by the white dots in Fig. 3d. These measurements can be accurately fit (RMSE<0.2 at.%) and interpolated with the surface-source evaporation equation [5,16]. Fig. 3d shows the result of this fitting, with the Eu concentration varying from 0.6 at.% to 8.6 at.%. X-ray diffraction measurements (Fig. S3) show that the AlN film has a hexagonal wurtzite structure, with a preferential growth direction.

Fig. 4a provides the excitation-emission map taken at an arbitrary location [(x,y) = (30 mm, 40 mm)] on the film. Fig. 4a shows that AlN:Eu^{3+} produces red emission when excited from 210 nm to 420 nm. The multiple emission lines are all resultant from 4f-4f emission of Eu^{3+}. The relative intensities of the emission lines are the same for all excitation wavelengths, and all emission lines have the same excitation spectrum, which is a strong indication that Eu^{3+} occupies a single site within the AlN lattice. A closer look at the strongest emission at 622 nm (indicated by the blue line in Fig. 4a), displayed in Fig. 4b, shows that the excitation can be clearly resolved in 3 Gaussian bands. The 0.53 eV wide (FWHM) band, centered at 3.54 eV (~ 350 nm) can be attributed to the charge transfer (CT) band from the valence band of AlN to Eu^{3+} [17,18]. The CT band is the energy required to displace an electron from a neighboring nitride (valence) anion onto Eu^{3+}, therefore

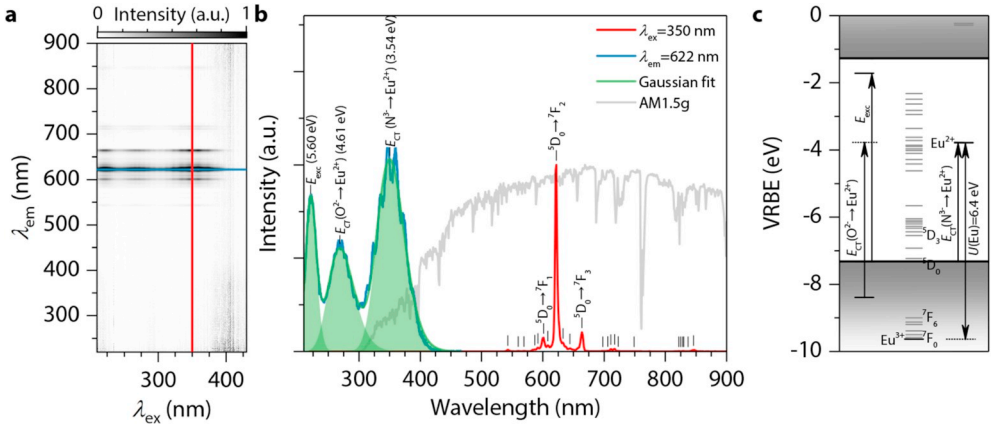

Fig. 4. Luminescent properties of the AlN:Eu^{3+} library. a) Simultaneous emission and excitation mapping of the photoluminescence of the AlN:Eu^{3+} thin film. Around 400 nm the noise increases due to low laser power. b) Excerpt taken at the blue and red lines from panel a. The gray curve shows the photon counts of the solar spectrum. Green surfaces are Gaussian fits to the three bands. c) Vacuum referred binding energy diagram for the AlN:Eu^{3+} thin film. Dashes for the separate 4f levels of Eu^{3+} are merely indicative and not at absolute energy scale. (For interpretation of the references to color in this figure legend, the reader is referred to the Web version of this article.)

providing the energy difference between the valence band and the Eu^{2+} ground state [19], shown by the arrow marked $E_{CT}(N^{3-} \rightarrow Eu^{2+})$ in Fig. 4c. The 0.52 eV wide band at $E_{exc} = 5.60$ eV ($\sim$ 221 nm) can be attributed to the creation of an exciton. The optical bandgap for the thin film AlN:Eu is 6.05 eV wide, 8% above the exciton energy [20], in agreement with Ref. [21].

With these properties, a vacuum referred binding energy (VRBE) diagram can be constructed [22]. Such a diagram is helpful in elucidating how the energy levels of defects compare to the same defects in other hosts. Based on what is reported for other nitride-type materials [23], the energy difference U(Eu) between Eu^{3+} and Eu^{2+} is taken at 6.4 eV. Using the relation [24]

$$E_{VRBE}(Eu^{2+}) = -24.92 + \frac{18.05 - U(Eu)}{0.777 - 0.0353U(Eu)}$$

the energy level of the 4f ground state of Eu^{2+} in relation to the vacuum can be placed. This placement leads to the VRBE diagram shown in Fig. 4c.

The 0.84 eV wide Gaussian at 4.61 eV (269 nm) is also placed in Fig. 4c. The $O^{2-} \rightarrow Eu^{2+}$ CT band is usually positioned around 4.7 eV in aluminates [19]. Therefore, since the thin film is produced in an environment containing O_2, the band at 4.61 eV can most likely be attributed to the $O^{2-} \rightarrow Eu^{2+}$ CT band.

When comparing Fig. 3b with Fig. 3c and d, we see that the AlN:Eu^{3+} library presents local maxima in emission intensity (indicated by the white dashed line) at different thicknesses and Eu concentrations. When following the white dashed line shown in Fig. 3b, we can observe that the thicker the film, the lower the optimum Eu concentration. These optima imply that for each thickness within the film there is a balance between quantum yield and absorption strength, as shown schematically in Fig. 1b. To evaluate if these optima translate to an optimum for LSC functionality, the absorption of light and quantum yield are resolved as a function of film thickness and Eu concentration in the next section.

To retrieve the concentration-dependent index of refraction n and molar absorption coefficient ε, the measured transmittance is fit to the thin film transmittance equation [25] for every measured wavelength. From this equation, ε can be derived from the extinction coefficient k with

$$\varepsilon_{Eu} = \frac{4\pi k_{Eu}}{\lambda c_{Eu}},$$

where k is assumed to scale with the Eu concentration c_{Eu} (in at.%) as

$$k = k_{Eu}c_{Eu} + k_{AlN}(100 \text{ at. \%} - c_{Eu}) .$$

This type of fitting yields n and ε, as presented in Fig. 5a for both undoped and Eu doped AlN. In the Supplementary Materials (Section S1, Figs. S4 and S5) a more in-depth explanation is given on how the fittings are done.

For undoped AlN, an index of refraction of $n = 1.90$ is found at $\lambda = 622$ nm. An increase in Eu concentration goes paired with an increase in refractive index, from $n = 1.92$ at 0.9 at.% to $n = 1.96$ at 6.7 at.% (Fig. 5b). The molar absorption coefficient of Eu^{3+} in AlN (Fig. 5a) shows the same bands as observed in the excitation spectrum (Fig. 4b). The $N^{3-} \rightarrow Eu^{2+}$ CT band at 350 nm has a molar absorption coefficient of 499 $cm^{-1}at.\%^{-1}$. In absorption, the bands have a different relative intensity than in excitation. This difference in intensity can come from different relaxation pathways for the different CT transitions. A different relaxation pathway goes associated with a different quantum yield, which alters the intensity of the band in excitation, where only radiative relaxation can be measured.

Fig. 5a reveals that doping Eu in AlN slightly alters the absorption of AlN itself. AlN is mostly reported to have no absorption for wavelengths larger than 400 nm [26], while in our films the absorption extends to longer wavelengths. It might therefore be that our film contains defects that may be removed when e.g. growing the film at elevated temperatures or annealing in a $N_2 + H_2$ atmosphere. Given the emissions as reported in Fig. 4a, Eu exhibits no self-absorption and the emission is not absorbed by the AlN host either.

The quantum yield η_{QY} can be estimated from the decay spectra, shown in Fig. 6a. In the first hundred nanoseconds a very quick decay can be observed. After this initial quick drop, the decay for any concentration in the library shows strong non-exponential behavior. As seen in Fig. 6a for selected concentrations, and in Fig. 6b for the entire library, the decay time decreases at higher Eu concentrations. Given the faster decays at higher concentrations, this effect can be explained by concentration quenching.

The data presented in Fig. 6b is collected at 20 × 20 locations across the film, which gives multiple data points for a specific concentration. These data come from areas with markedly different thicknesses. No relation between decay time and thickness is found, confirming that the decay time solely depends on the dopant concentration. The good correspondence between measured decay time and the interpolated Eu concentration (Fig. 3d) also confirms the correctness of the EDX measurements and the usage of the source-surface evaporation equation.

To obtain η_{QY} per concentration, the decay can be compared to decays reported at much lower concentrations, where concentration quenching can be excluded [27]. report a decay of $\tau = 428$ μs for an AlN:Eu^{3+} thin film doped with 5 ppm Eu. This low-concentration Eu film does not show thermal quenching of the intensity of cathodoluminescence. This implies that in the film of Jadwisienczak et al. both concentration-quenching and thermal-related quenching behavior can be excluded. Therefore, when assuming the decay of 428 μs corresponds to $\eta_{QY} = 1$, η_{QY} in our thin film can be estimated as

$$\eta_{QY} = \frac{\tau_{mean}}{\tau},$$

with $\tau_{mean} = \frac{\int_{t=0}^{\infty} tI(t)\,dt}{\int_{t=0}^{\infty} I(t)\,dt}$ the average decay time. This average decay time

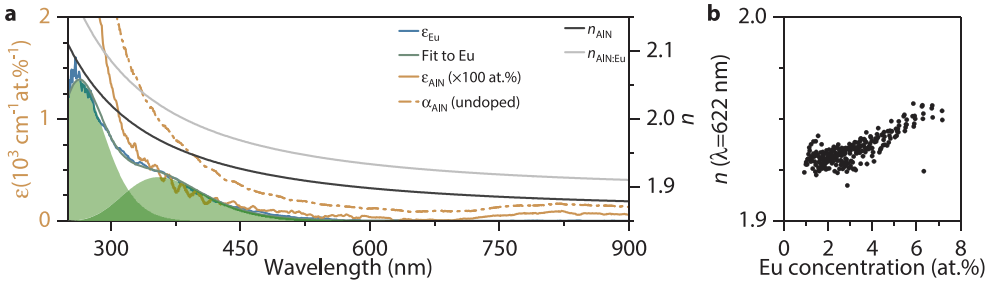

Fig. 5. a) Average index of refraction n, molar absorption coefficients ε for all wavelengths for both undoped AlN (average adj. $R^2 = 0.94$) as well as Eu doped AlN (average adj. $R^2 = 0.92$). α_{AlN} is the absorbance ($\varepsilon \times 100$ at.%) of AlN without a Eu doping. Green surfaces are Gaussian fits to ε_{Eu}, with the same centers as reported in Fig. 4b. These fits show the CT bands in the absorption of Eu. b) Index of refraction at 622 nm as a function of Eu concentration. (For interpretation of the references to color in this figure legend, the reader is referred to the Web version of this article.)

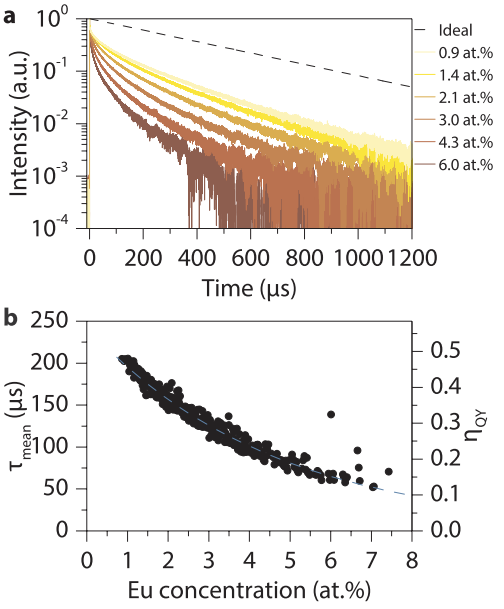

Fig. 6. Decay times across the substrate ($\lambda_{ex} = 350$ nm). a) Individual decay traces for different Eu concentrations. b) Mean decay times for all Eu concentrations on the thin film, with on the right y-axis the associated estimated η_{QY}. The dashed blue line shows the trend of τ_{mean}. (For interpretation of the references to color in this figure legend, the reader is referred to the Web version of this article.)

is largely uninfluenced by the fast decay in the first hundred nanoseconds, as the surface underneath the curve is negligible compared to the surface from the remaining hundreds of microseconds. Fig. 6b shows both τ_{mean} and the estimated η_{QY}. Even for a Eu doping as low as 1 at.%, AlN:Eu^{3+} does not exceed a quantum efficiency of 50%. From Fig. 6b, η_{QY} can be extrapolated to its value at 0 at.% Eu. Extrapolating the dashed curve would lead to $\eta_{QY}(0\text{ at. \%}) \neq 1$. In materials with a CT band at low energy, the CT state can overlap with the Eu^{3+} ground state [28]. This overlap with the Eu^{3+} ground state opens a temperature-independent non-radiative pathway for relaxation of the excited Eu to the ground state. In practice this means that even at 0 K, the quantum yield does not equal unity. The energy of the $N^{3-} \rightarrow Eu^{2+}$ CT band in AlN:Eu^{3+} is relatively low [comparable to $LaAlO_3$:Eu^{3+} (315 nm)]. It is therefore possible that, independent of temperature or Eu concentration, $\eta_{QY} \neq 1$ for AlN:Eu^{3+}. However, even for non-unity η_{QY} when $\tau_{mean} = \tau$, the method presented in this article is still valid. The results found here will then have to be multiplied by this non-unity quantum yield to obtain the correct efficiencies.

An optimum in optical efficiency for an AlN:Eu^{3+} LSC can now be retrieved, because the parameters required by Eq. (1) have been determined as a function of Eu concentration and film thickness, as will be detailed in the following.

As this study concerns a thin film, the amount of absorbed incident light cannot be calculated using geometrical optics. The transfer-matrix method [29] that takes multiple reflections at the interfaces of the thin film into account is used to calculate how much sunlight (AM1.5g) is absorbed. The absorbance and index of refraction reported by Fig. 5a are used to calculate the number of reflected, transmitted and absorbed solar photons. The amount of emission is calculated by multiplying the number of photons absorbed by Eu^{3+} by the estimated η_{QY} from Fig. 6b. Eu^{3+} is assumed to be distributed randomly in the AlN host. Therefore, we can safely assume light emitted by Eu^{3+} to be transported incoherently through the thin film and the substrate [30]. Thanks to this incoherent transport, geometrical optics can be used to calculate the light transport after emission. The amount of trapped light can be calculated by multiplying the number of emitted photons by $\eta_{trap}(\lambda = 622\text{ nm}) = 85.5\%$. This takes both transport through the film and through the glass substrate into account. A perfect (scatter-free) waveguide is assumed: $\eta_{WG} = 1$. Since no reabsorption of Eu^{3+} is present, $\eta_{SA} = 1$ and the efficiency optimization is irrespective of the overall LSC geometry [12].

Fig. 7a shows the result of this optimization. The percentages shown in Fig. 7a are the optical efficiencies of the LSC for AM1.5g solar

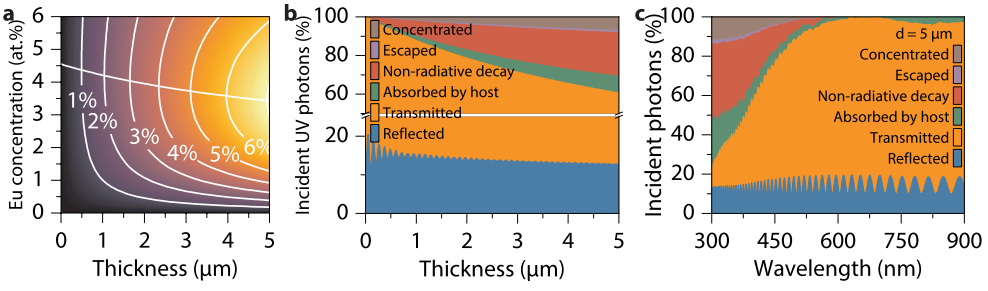

Fig. 7. Simulated optimization of an AlN:Eu^{3+} thin film LSC for maximal optical efficiency. a) Calculated optical efficiency for photons until 450 nm, as a function of both thickness and Eu concentration. The white line through the contour lines indicates the maximal optical efficiency per thickness. b) Eventual fate of all solar photons until 450 nm incident on the LSC, for the optimal concentrations as a function of thickness (white line in panel a). The photons that are concentrated are the photons responsible for the eventual power-output of the LSC. The oscillation between reflected and transmitted photons is a consequence of thin film interference. c) Fate of incident AM1.5g solar photons for an optimized 5 μm thick film.

photons until 450 nm. These photons constitute 7.7% of the total amount of photons in the solar spectrum. To retrieve the optical efficiency when considering the entire solar spectrum, the percentages reported in Fig. 7a should be multiplied with a factor 0.077. Fig. 7a reflects what was already observed in Fig. 3b: a higher concentration of Eu^{3+}, at equal film thickness, does not have to imply a higher optical efficiency. The white curve, drawn perpendicular to the contour lines, indicates the optimum concentration per thickness. This curve follows the behavior schematically sketched in Fig. 1b: at higher thickness, a lower Eu concentration is required to achieve optimal optical efficiency.

Fig. 7b details the distribution of the incident AM1.5g UV photons (integrated until 450 nm) for the optimized Eu concentrations at every thickness. At film thicknesses below 2 µm, the effect of thin film interference is evident in the transmission and reflection, with transmission being the most prevalent fate for an incident photon. With increasing film thicknesses, the reflection starts converging to what would be expected from geometrical optics, while the transmission drops drastically as a result of increased absorption. At the same time, the fraction of absorbed photons yielding luminescence increases for thicker films. This increase is a consequence of the lower Eu concentration an optimized LSC with a thicker film requires, hence resulting in less concentration quenching. However, even with this lowered quenching, only 7% of incoming UV photons will be converted and concentrated at the LSC's edges for a 5 µm thick film.

Fig. 7c provides a breakdown of the eventual fate of all incident solar photons for an optimized 5 µm thick LSC. The interference effect caused by a thin film can still be clearly observed from the oscillations between transmission and reflection. The effect of the $N^{3-} \rightarrow Eu^{2+}$ CT absorption (Fig. 5a) can also be observed, with most absorption and conversion resulting from this band. The high absorption from this CT band ($1697\ cm^{-1}$ at 350 nm) does not counteract the high non-radiative loss due to the low quantum yield of 27% at 3.4 at.% Eu doping.

In an idealized case, where the dashed curve displayed in Fig. 6b is scaled such that $\eta_{QY} = 1$ at 0 at.% Eu, illustrated in the Supplementary Materials (Section S2, Fig. S6), 3.4 at.% Eu doping has $\eta_{QY} = 47\%$. In this idealized case, 13% of the incident UV photons will be concentrated at the LSC's edges for a 5 µm thick film. The goal of this study is however to present a method where experimental data from a luminescence library is used to model, understand, and optimize a thin film LSC, not to produce an LSC of high efficiency. Even so, to put the efficiency of this simulated AlN:Eu^{3+} thin film LSC into perspective, a comparison can be drawn to other emerging UV-absorbing LSCs without self-absorption. A recent example of such a UV-absorbing LSC are perovskite nanocrystals doped with Mn^{2+} dissolved in a polymer matrix, laminated on glass. The absorptance of these laminated nanocrystals lies between 1 and $2\ cm^{-1}$ [4]. These perovskites have non-overlapping absorption (until 400 nm) and emissions (maximal at 600 nm), comparable to AlN:Eu^{3+}. Given the low absorptance, these perovskites require much thicker (~ 1 mm thick) films to achieve absorption equivalent to a 1 µm thick AlN:Eu^{3+} film. Even with such thick films, the nanocrystals' low quantum yields culminates into an LSC of low efficiency. Compared to these nanocrystals, rare earth doped thin films show their potential as LSC due to their high absorptivity. Rare earth doped thin films are compatible with industrial fabrication processes, and, with materials that exhibit a lower degree of concentration quenching, can yield an LSC with a high optical efficiency.

4. Conclusion

We have shown that using the deposition of a single thin film, it is possible to calculate the thickness-dependent optimum dopant concentration of a thin film LSC, yielding a maximized optical efficiency. As a model system, we have fabricated an AlN:Eu^{3+} library co-doped with O^{2-}. The library shows red 4f-4f emission after UV excitation and features a large thickness- and Eu^{3+} concentration gradient. Optimization shows that a 5 µm thick film performs best with 3.4 at.% Eu doping. This combination would yield an optimal optical efficiency for incoming UV light of 7%. The fabrication and optimization method presented in this paper can assist in quickly finding the maximally achievable performance for a self-absorption free thin film LSC.

Acknowledgements

The authors would like to thank P. Dorenbos and H.T. Hintzen for valuable discussions and A. Golova for proofreading the manuscript. This work was supported by the Netherlands Organisation for Scientific Research (NWO/OCW), as part of the Frontiers of Nanoscience program (NF16NFS01) and as part of the LumiCon project (15024).

Appendix A. Supplementary data

Supplementary data to this article can be found online at https://doi.org/10.1016/j.solmat.2019.110032.

References

[1] W.H. Weber, J. Lambe, Luminescent greenhouse collector for solar radiation, Appl. Optic. 15 (10) (1976) 2299–2300, https://doi.org/10.1364/AO.15.002299 https://www.osapublishing.org/ao/abstract.cfm?uri=ao-15-10-2299 ISSN 0003-6935.

[2] C.S. Erickson, L.R. Bradshaw, S. McDowall, J.D. Gilbertson, D.R. Gamelin, D.L. Patrick, Zero-reabsorption doped-nanocrystal luminescent solar concentrators, ACS Nano 8 (4) (2014) 3461–3467, https://doi.org/10.1021/nn406360w ISSN 1936-0851 http://pubs.acs.org/doi/abs/10.1021/nn406360w.

[3] Y. Zhao, R.R. Lunt, Transparent luminescent solar concentrators for large-area solar windows enabled by massive Stokes-shift nanocluster phosphors, Adv. Energy Mater. 3 (9) (2013) 1143–1148, https://doi.org/10.1002/aenm.201300173 ISSN 16146832 http://doi.wiley.com/10.1002/aenm.201300173.

[4] F. Meinardi, Q.A. Akkerman, F. Bruni, S. Park, M. Mauri, Z. Dang, L. Manna, S. Brovelli, Doped halide perovskite nanocrystals for reabsorption-free luminescent solar concentrators, ACS Energy Letters 2 (10) (2017) 2368–2377, https://doi.org/10.1021/acsenergylett.7b00701 ISSN 23808195 https://pubs.acs.org/doi/pdf/10.1021/acsenergylett.7b00701.

[5] E.P.J. Merkx, E. van der Kolk, Method for the detailed characterization of co-sputtered inorganic luminescent material libraries, ACS Comb. Sci. (2018) 2156–8952, https://doi.org/10.1021/acscombsci.8b00068 acscombsci.8b00068ISSN https://pubs.acs.org/sharingguidelineshttp://pubs.acs.org/doi/10.1021/acscombsci.8b00068.

[6] G. Bräuer, B. Szyszka, M. Vergöhl, R. Bandorf, Magnetron sputtering – milestones of 30 years, Vacuum 84 (12) (2010) 1354–1359, https://doi.org/10.1016/j.vacuum.2009.12.014 ISSN 0042207X http://linkinghub.elsevier.com/retrieve/pii/S0042207X10000163.

[7] M. Peres, A. Cruz, M. Soares, A. Neves, T. Monteiro, K. Lorenz, E. Alves, Optical and structural studies in Eu-implanted AlN films, Superlattice. Microst. 40 (4–6) (2006) 537–544, https://doi.org/10.1016/j.spmi.2006.07.031 ISSN 07496036 http://linkinghub.elsevier.com/retrieve/pii/S0749603606000966.

[8] J.B. Gruber, U. Vetter, T. Taniguchi, G.W. Burdick, H. Hofsäss, S. Chandra, D.K. Sardar, Spectroscopic analysis of Eu^{3+} in single-crystal hexagonal phase AlN, J. Appl. Phys. 110 (2) (2011), https://doi.org/10.1063/1.3609076 023104, ISSN 0021-8979 http://aip.scitation.org/doi/10.1063/1.3609076.

[9] K. Wang, K.P. O'Donnell, B. Hourahine, R.W. Martin, I.M. Watson, K. Lorenz, E. Alves, Luminescence of Eu ions in $Al_xGa_{1-x}N$across the entire alloy composition range, Phys. Rev. B 80 (12) (2009) 125206, https://doi.org/10.1103/PhysRevB.80.125206 ISSN 1098-0121 https://link.aps.org/doi/10.1103/PhysRevB.80.125206.

[10] M. Maqbool, W.M, M.E, Cathodoluminescence from amorphous and nanocrystalline nitride thin films doped with rare earth and transition metals, Cathodoluminescence, InTech, 2012, , https://doi.org/10.5772/34869 http://www.intechopen.com/books/cathodoluminescence/cathodoluminescence-from-amorphous-and-nano-crystalline-nitride-and-oxide-thin-films-doped-with-rare.

[11] M. Maqbool, Luminescence and thermal annealing of sputtered deposited thulium- and samarium-doped amorphous AlN films, 05n06, Surf. Rev. Lett. 12 (2005) 767–771, https://doi.org/10.1142/S0218625X05007633 ISSN 0218-625X http://www.worldscientific.com/doi/abs/10.1142/S0218625X05007633.

[12] E.P.J. Merkx, O.M. ten Kate, E. van der Kolk, Rapid optimization of large-scale luminescent solar concentrators: evaluation for adoption in the built environment, Optic Express 25 (12) (2017), https://doi.org/10.1364/OE.25.00A547 A547, ISSN 1094-4087 https://www.osapublishing.org/abstract.cfm?URI=oe-25-12-A547.

[13] D.L. Dexter, J.H. Schulman, Theory of concentration quenching in inorganic phosphors, J. Chem. Phys. 22 (6) (1954) 1063–1070, https://doi.org/10.1063/1.1740265 ISSN 0021-9606 https://aip.scitation.org/doi/10.1063/1.1740265.

[14] M.L. Caldwell, P.G. Van Patten, M.E. Kordesch, H.H. Richardson, Visible luminescent activation of amorphous AlN:Eu thin-film phosphors with oxygen, MRS Internet J. Nitride Semicond. Res. 6 (13) (2001), https://doi.org/10.1557/S1092578300000259 e13, ISSN 1092-5783 https://www.cambridge.org/core/journals/materials-research-society-internet-journal-of-nitride-semiconductor-

research/article/visible-luminescent-activation-of-amorphous-alneu-thinfilm-phosphors-with-oxygen/7608AB82CE3CA1AD92A84D990C6C88E4.
[15] E.P.J. Merkx, S. van Overbeek, E. van der Kolk, Functionalizing window coatings with luminescence centers by combinatorial sputtering of scatter-free amorphous SiAlON:Eu^{2+} thin film composition libraries, J. Lumin. 208 (2019) 51–56, https://doi.org/10.1016/j.jlumin.2018.12.011 ISSN 00222313 https://www.sciencedirect.com/science/article/pii/S0022231318314583.
[16] J.D. Fowlkes, J.M. Fitz-Gerald, P.D. Rack, Ultraviolet emitting (Y1-xGdx)2O3-δ thin films deposited by radio frequency magnetron sputtering: combinatorial modeling, synthesis, and rapid characterization, Thin Solid Films 510 (1–2) (2006) 68–76, https://doi.org/10.1016/j.tsf.2005.12.309 ISSN 00406090 http://www.sciencedirect.com/science/article/pii/S0040609006000435.
[17] P. Dorenbos, E. van der Kolk, Location of lanthanide impurity energy levels in the III-V semiconductor $Al_xGa1_xN(0 \leq x \leq 1)$, ISSN 09253467, Opt. Mater. 30 (7) (2008) 1052–1057, https://doi.org/10.1016/j.optmat.2007.05.019 http://linkinghub.elsevier.com/retrieve/pii/S0925346707001565.
[18] T. Shibata, K. Asai, S. Sumiya, M. Mouri, M. Tanaka, O. Oda, H. Katsukawa, H. Miyake, K. Hiramatsu, High-quality AlN epitaxial films on (0001)-faced sapphire and 6H-SiC substrate, Phys. Status Solidi 2026 (7) (2003) 2023–2026, https://doi.org/10.1002/pssc.200303392 ISSN 1610-1634 http://doi.wiley.com/10.1002/pssc.200303392.
[19] P. Dorenbos, Charge transfer bands in optical materials and related defect level location, Opt. Mater. 69 (8–22) (2017), https://doi.org/10.1016/j.optmat.2017.03.061 ISSN 09253467 http://linkinghub.elsevier.com/retrieve/pii/S0925346717302082.
[20] P. Dorenbos, The Eu^{3+} charge transfer energy and the relation with the band gap of compounds, J. Lumin. 111 (1–2) (2005) 89–104, https://doi.org/10.1016/j.jlumin.2004.07.003 ISSN 00222313 https://www.sciencedirect.com/science/article/pii/S0022231304002364.
[21] Q. Guo, A. Yoshida, Temperature dependence of band gap change in InN and AlN, Part 1, No. 5A, Jpn. J. Appl. Phys. 33 (1994) 2453–2456, https://doi.org/10.1143/JJAP.33.2453 ISSN 0021-4922 https://www.sciencedirect.com/science/article/pii/S0022231304002364 http://stacks.iop.org/1347-4065/33/2453.
[22] P. Dorenbos, E. van der Kolk, Lanthanide impurity level location in GaN, AlN, and ZnO, in: H. Morkoc, C.W. Litton (Eds.), Gallium Nitride Materials and Devices II, 647313, 2007, https://doi.org/10.1117/12.698977 http://proceedings.spiedigitallibrary.org/proceeding.aspx?doi=10.1117/12.698977.
[23] P. Dorenbos, Relation between Eu^{2+} and Ce^{3+} f →d-transition energies in inorganic compounds, J. Phys. Condens. Matter 15 (27) (2003) 4797–4807, https://doi.org/10.1088/0953-8984/15/27/311 ISSN 09538984 https://iopscience.iop.org/article/10.1088/0953-8984/15/27/311.
[24] P. Dorenbos, Determining binding energies of valence-band electrons in insulators and semiconductors via lanthanide spectroscopy, Phys. Rev. B 87 (3) (2013) 035118, , https://doi.org/10.1103/PhysRevB.87.035118 ISSN 1098-0121 https://link.aps.org/doi/10.1103/PhysRevB.87.035118.
[25] R. Swanepoel, Determination of the thickness and optical constants of amorphous silicon, J. Phys. E Sci. Instrum. 16 (12) (1983) 1214–1222, https://doi.org/10.1088/0022-3735/16/12/023 ISSN 0022-3735 https://iopscience.iop.org/article/10.1088/0022-3735/16/12/023.
[26] S. Adachi, Optical Constants of Crystalline and Amorphous Semiconductors: Numerical Data and Graphical Information, Springer US, Boston, MA, 1999, https://doi.org/10.1007/978-1-4615-5247-5 ISBN 0792385675 http://link.springer.com/10.1007/978-1-4615-5247-5.
[27] W.M. Jadwisienczak, H.J. Lozykowski, I. Berishev, A. Bensaoula, I.G. Brown, Visible emission from AlN doped with Eu and Tb ions, J. Appl. Phys. 89 (8) (2001) 4384–4390, https://doi.org/10.1063/1.1357467 ISSN 0021-8979 http://aip.scitation.org/doi/10.1063/1.1357467.
[28] G. Blasse, A. Bril, J.A. de Poorter, Radiationless transitions in the Eu^{3+} center in $LaAlO_3$, J. Chem. Phys. 53 (12) (1970) 4450–4453, https://doi.org/10.1063/1.1673972 ISSN 0021-9606 http://aip.scitation.org/doi/10.1063/1.1673972.
[29] S.J. Byrnes, Multilayer Optical Calculations, http://arxiv.org/abs/1603.02720.
[30] J. Gutmann, M. Peters, B. Bläsi, M. Hermle, A. Gombert, H. Zappe, J.C. Goldschmidt, Electromagnetic simulations of a photonic luminescent solar concentrator, Optic Express 20 (S2) (2012), https://doi.org/10.1364/OE.20.00A157 A157, ISSN 1094-4087 https://www.osapublishing.org/abstract.cfm?URI=oe-20-S2-A157.